PHYSICAL REVIEW D **88,** 034501 (2013)

Quark propagation in the instantons of lattice QCD

Amalie Trewartha,* Waseem Kamleh, Derek Leinweber, and Dale S. Roberts
Centre for the Subatomic Structure of Matter, School of Chemistry and Physics, University of Adelaide, South Australia 5005, Australia
(Received 18 June 2013; published 7 August 2013)

We quantitatively examine the extent to which instanton degrees of freedom, contained within standard Monte-Carlo generated gauge-field configurations, can maintain the characteristic features of the mass and renormalization functions of the nonperturbative quark propagator. We use over-improved stout-link smearing to isolate instanton effects on the lattice. Using a variety of measures, we illustrate how gauge fields consisting almost solely of instantonlike objects are produced after only 50 sweeps of smearing. We find a full vacuum, with a packing fraction more than three times larger than phenomenological models predict. We calculate the overlap quark propagator on these smeared configurations, and find that even at high levels of smearing the majority of the characteristic features of the propagator are reproduced. We thus conclude that instantons contained within standard Monte-Carlo generated gauge-field configurations are the degrees of freedom responsible for the dynamical generation of mass observed in lattice QCD.

DOI: 10.1103/PhysRevD.88.034501 PACS numbers: 11.30.Rd, 12.38.Gc, 14.70.Dj

I. INTRODUCTION

Instantons are believed to be an essential component of the long-distance physics of the QCD vacuum, and the lattice provides a unique opportunity to gain insight into their role. In this study, we will for the first time quantitatively examine the extent to which instanton degrees of freedom, contained within standard Monte-Carlo generated gauge-field configurations, can maintain the characteristic features of the mass and renormalization functions of the nonperturbative quark propagator.

In order to isolate the effects of instanton degrees of freedom, a UV filter is required to remove topologically non-trivial fluctuations. A variety of filters have been used, including cooling [1–3], APE smearing [4], HYP smearing [5] and stout link smearing [6], among others. These algorithms can suffer from destruction of the instanton content of the vacuum, and so in this work we use over-improved stout-link smearing [7,8], a form of smearing tuned to preserve instantons. Section II briefly describes these smearing methods.

We then seek to quantify the effects of smearing on the lattice gauge fields in Sec. III. We produce configurations dominated by instantonlike objects, and compare to the phenomenological instanton liquid model [9–11], which models the vacuum as composed of a constant number of instantons and anti-instantons of constant radius.

We will then briefly introduce the Fat Link Irrelevant Clover(FLIC) overlap action [12] in Sec. IV, an improved fermion action with a lattice deformed version of chiral symmetry, which removes the problem of additive mass renormalization of the quark propagator. Results will be compared for smeared and unsmeared configurations in Sec. V, and conclusions summarized in Sec. VI.

*AmalieTrewartha@lbl.gov

II. OVER-IMPROVED STOUT-LINK SMEARING

It has long been known [2,3,13] that smearing the lattice reveals objects which approximate classical instantons. However, it has been known for nearly as long that excessive smearing can destroy the same instantonlike objects or distort their structure.

We can understand this behavior by explicitly considering the single instanton solution, [14–17]

$$A_\mu(x,x_0) = \frac{i}{g}\frac{(x-x_0)^2}{(x-x_0)^2+\rho^2}(\delta_\mu S)S^{-1}, \qquad S = \frac{x_4 \pm i\vec{x}.\vec{\sigma}}{\sqrt{x^2}}, \tag{1}$$

where ρ is the instanton radius, σ the Pauli matrices and x_0 the center of the instanton. The Wilson gauge action can be expanded in powers of a as [7]

$$\begin{aligned} S_W = \sum_{x,\mu,\nu}\mathrm{Tr}\Big[& -\frac{a^4}{2}F_{\mu\nu}^2 + \frac{a^6}{24}((\mathbf{D}_\mu F_{\mu\nu}(x))^2 + (\mathbf{D}_\nu F_{\mu\nu}(x))^2) \\ & - \frac{a^8}{24}\Big\{F_{\mu\nu}^4(x) + \frac{1}{30}((\mathbf{D}_\mu^2 F_{\mu\nu}(x))^2 \\ & + (\mathbf{D}_\nu^2 F_{\mu\nu}(x))^2) + \frac{1}{3}\mathbf{D}_\mu^2 F_{\mu\nu}(x)\mathbf{D}_\nu^2 F_{\mu\nu}(x) \\ & - \frac{1}{4}(\mathbf{D}_\mu\mathbf{D}_\nu F_{\mu\nu}(x))^2\Big\}\Big], \end{aligned} \tag{2}$$

where $\mathbf{D}_\mu f = [D_\mu, f]$ for arbitrary f.

Inserting the instanton solution of Eq. (1) into Eq. (2), we acquire

$$S_w^{\mathrm{inst}} = \frac{8\pi^2}{g^2}\left[1 - \frac{1}{5}\left(\frac{a}{\rho}\right)^2 - \frac{1}{70}\left(\frac{a}{\rho}\right)^4 + \mathcal{O}(a^6)\right]. \tag{3}$$

The source of the problem is clear; although at first order this is equal to the continuum instanton action, the leading order error term is strictly negative and inversely

 © 2013 American Physical Society

proportional to ρ. The use of a plaquette-based smearing algorithm will reduce the size of instantons in decreasing the action and ultimately enable lattice artifacts to spoil and remove the instanton. This situation is not ameliorated by using improved actions such as the Symanzik action [7].

This issue can be mitigated using over-improved stout-link smearing, a form of smearing designed to preserve instantons. This was first implemented in Ref. [7], although here we follow the work Ref. [8], which uses a slightly modified combination of links. One introduces a new parameter ϵ, defining

$$S(\epsilon) = \frac{2}{g^2}\sum_x \sum_{\mu>\nu}\left[\frac{5-2\epsilon}{3}(1-P_{\mu\nu}) - \frac{1-\epsilon}{12}(1-R_{\mu\nu})\right], \tag{4}$$

with $P_{\mu\nu}$ and $R_{\mu\nu}$ the 1×1 and 1×2 plaquettes. We note that a value of $\epsilon = 1$ gives the Wilson plaquette action and $\epsilon = 0$ gives the Symanzik improved action [18]. Again substituting the instanton solution into this, one acquires [8]

$$S^{\text{inst}}(\epsilon) = \frac{8\pi^2}{g^2}\left[1 - \frac{\epsilon}{5}\left(\frac{a}{\rho}\right)^2 + \frac{14\epsilon - 17}{210}\left(\frac{a}{\rho}\right)^4\right]. \tag{5}$$

A negative value of ϵ will preserve instantonlike objects by making the first-order error term positive. This has however, simultaneously introduced a new problem; we have removed the possibility of shrinking objects and replaced it with that of enlarging, and so smearing can distort the topological structure of the lattice if used excessively with large negative values of ϵ. Following Ref. [8], we adopt the small value $\epsilon = -0.25$.

Explicitly, a sweep of over-improved stout-link smearing is implemented by replacing all links on the lattice with a smeared link, defined by

$$U'_\mu(x) = \exp(iQ_\mu(x))U_\mu(x), \tag{6}$$

where

$$Q_\mu(x) = \frac{i}{2}(\Omega^\dagger_\mu(x) - \Omega_\mu(x)) - \frac{i}{2N}\,\text{Tr}(\Omega^\dagger_\mu(x) - \Omega_\mu(x)), \tag{7}$$

with

$$\Omega_\mu(x) = C_\mu(x)U^\dagger_\mu(x). \tag{8}$$

Then we define

$$C_\mu(x) = \rho\sum_\nu\left[\frac{5-2\epsilon}{3}(\Xi_{\mu\nu})(x) - \frac{1-\epsilon}{12}(L_{\mu\nu}(x))\right], \tag{9}$$

where ρ is a parameter controlling the level of smearing and $\Xi_{\mu\nu}$ are "staples"; the 3 links in the $\mu\nu$ plane forming the $P_{\mu\nu}$ plaquette with U_μ removed, and $L_{\mu\nu}$ are analogously defined for 2×1 rectangles, illustrated in Fig. 1.

Following the work in Ref. [8], we choose $\rho = 0.06$ and $\epsilon = -0.25$, as these provide values of $S(\epsilon)/S_{\text{continuum}}$ close to 1, and preserve instantonlike objects on the lattice with

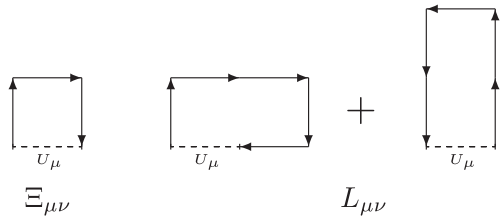

FIG. 1. Components of $\Xi_{\mu\nu}$ and $L_{\mu\nu}$.

size above the dislocation threshold of $1.97a$. We note however, that small objects can still be destroyed by the smearing process. Pair annihilation can also remove them from the lattice.

III. EFFECTS OF SMEARING

We wish to find a smearing level such that the configurations are dominated by topological objects as similar to continuum instantons as possible. At the same time, one needs to be wary of distorting their topological structure by enlarging or pair annihilating these objects. We will quantify the effects of smearing in order to choose an optimal balance between these two effects.

The work in Ref. [19] suggests that after just 20 sweeps of over-improved stout-link smearing, topological objects found on the lattice closely approximate instantons. Here we adopt a similar approach to that taken in Ref. [19], searching the lattice for sites which are local maxima of the action in their surrounding hypercube [15]. These are then taken as the approximate center of an (anti-)instanton, around which we fit the classical instanton action density,

$$S_0(x) = \xi\frac{6}{\pi^2}\frac{\rho^4}{((x-x_0)^2+\rho^2)^4}, \tag{10}$$

where ξ, ρ and x_0 are fit parameters, noting that x_0 is not restricted to lattice sites. The parameter ξ is introduced as lattice topological objects are expected to have a higher action than classical instantons. We wish to determine the fit by using the shape of the action density around a local maximum, rather than the height. We can then compare data obtained for the radii, ρ, of instanton candidates from this to the relationship between the radius and topological charge at the center of an (anti-)instanton.,

$$q(x_0) = Q\frac{6}{\pi^2\rho^4}, \tag{11}$$

where $Q = \mp 1$ for an (anti-)instanton. $q(x_0)$ at the fitted values of x_0 are found using linear interpolation from neighboring hypercubes to find an extremum inside the hypercube containing x_0. This data will provide the basis for our investigation of the effects of smearing.

Simulations are performed on 50 dynamical FLIC $20^3\times 40$ configurations, with a lattice spacing of 0.126 fm, corresponding to a spatial extent of 2.52 fm. Periodic boundary conditions are used. Up to 300 sweeps of smearing are investigated. To calculate the action and

topological charge densities used in our fits we use the $\mathcal{O}(a^4)$ five-loop improved action and charge densities defined in Ref. [20].

It should be noted that at low levels of smearing we expect to fit a large number of false positives; local maxima of the action corresponding to noise. The degree to which fitted results concur with Eq. (11) will thus be a key first test. This correspondence is graphed for a single configuration in Fig. 2 for various smearing levels. The number of instanton candidates starts out large and distributed fairly evenly around sizes of 2–8 lattice units, with little correlation to the predicted charge lines of Eq. (11). This quickly changes as the number of smearing sweeps increases, eventually leading to a very close fit. The number of instanton candidates also drops off rapidly at first, then steadily decreases. By the 50 sweep mark we can be confident that almost all local maxima found closely approximate an instanton near the center. Notably, instanton candidates with low radii have systematically lower topological charge at the center than predicted by Eq. (11). This is due to their proximity to the dislocation threshold of $1.97a$, under which objects are shrunk.

We define the squared distance from the theoretical relationship of Eq. (11), D^2_{TR}, as the minimum distance of each point from the theoretical relationship, i.e., for an instanton candidate with radius ρ_0 and topological charge at the centre q_0,

$$D^2_{\mathrm{TR}} = \min_{\rho}\left[(\rho-\rho_0)^2 + \left(\frac{\pm 6}{\pi^2\rho^4} - q_0\right)^2\right]. \quad (12)$$

The average value of this is plotted for data from 10 configurations in Fig. 3, as a function of the number of sweeps of overimproved smearing, $\mathrm{N_{sw}}$. This confirms our earlier observations; before 50 sweeps, D^2_{TR} decreases very rapidly as noise is removed from the lattice. After 50 sweeps, the decrease is characteristically slower.

We have seen in Eq. (5) that smearing carries the risk of distorting the vacuum structure by enlarging topological objects. This concern is confirmed in Fig. 4, illustrating the average radius of instanton candidates as a function of smearing. After an initial rapid drop, attributable to false positives being rapidly removed by the smearing algorithm, there is a small but steady increase in the average radius of the instanton candidates found.

In Fig. 5, we plot the average density of instanton candidates, N_{inst}/V, where N_{inst} is the number of instanton candidates found on a configuration and V the lattice volume. This shows a rapid decrease until around 70 sweeps in the early stages of smearing as false positives are rapidly eliminated. Eventually, instanton/anti-instanton annihilation becomes the dominant factor, slowing as the population becomes sparse. Again, the regime of 50 sweeps characterizes this transition. Also of note is the

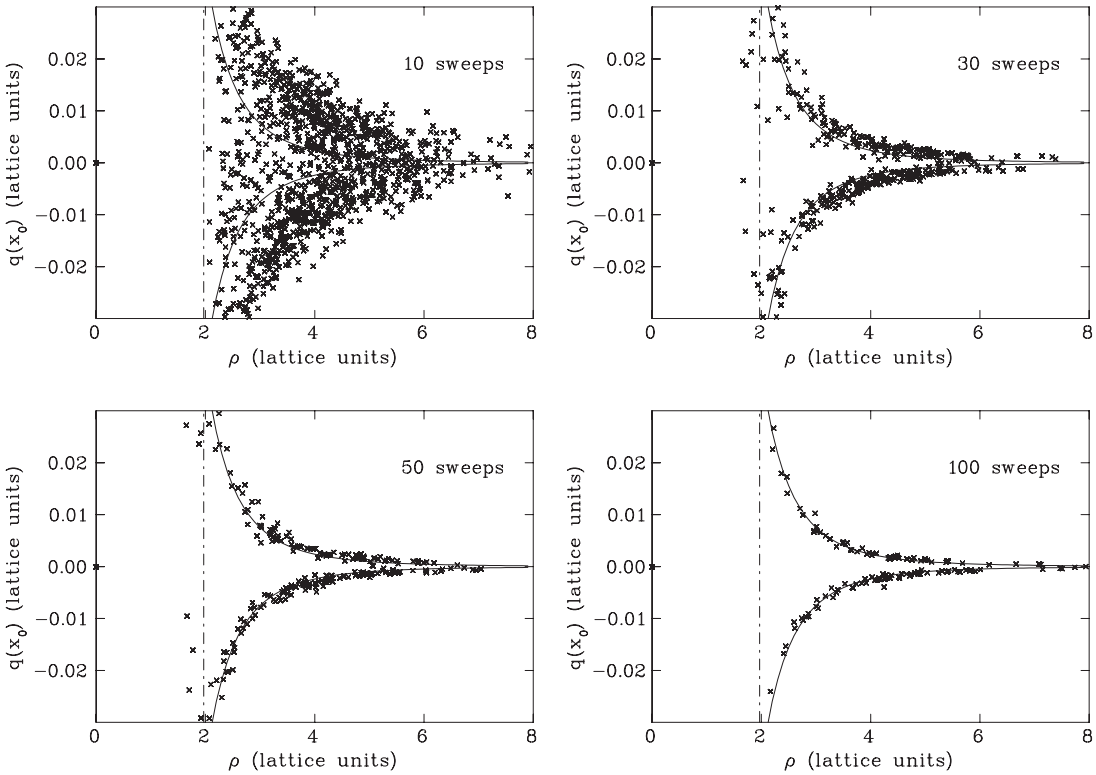

FIG. 2. The values of the instanton radius ρ, found by fitting lattice maxima of the action to the classical instanton action density of Eq. (10) are plotted as crosses, against the topological charge at the center, $q(x_0)$, on configurations with 10, 30, 50 and 100 sweeps of smearing. Results are compared to the theoretical relationship between the instanton radius and topological charge at the center, Eq. (11) (solid lines), and the dislocation threshold, $1.97a$ (dash-dotted line).

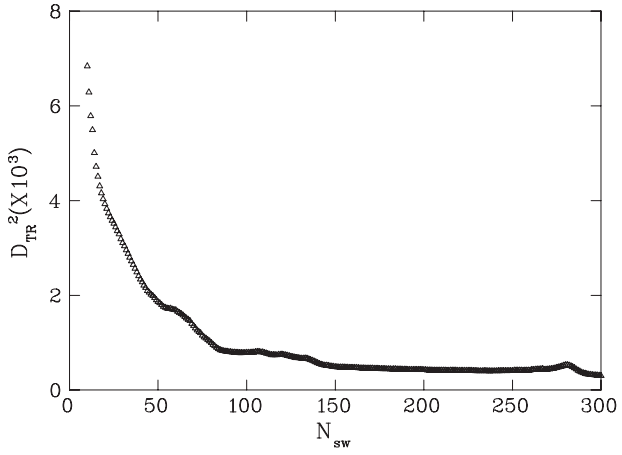

FIG. 3. Average squared distance from the theoretical relation, D^2_{TR}, between topological charge at the center of an instanton candidate and its fitted radius, as a function of smearing sweeps.

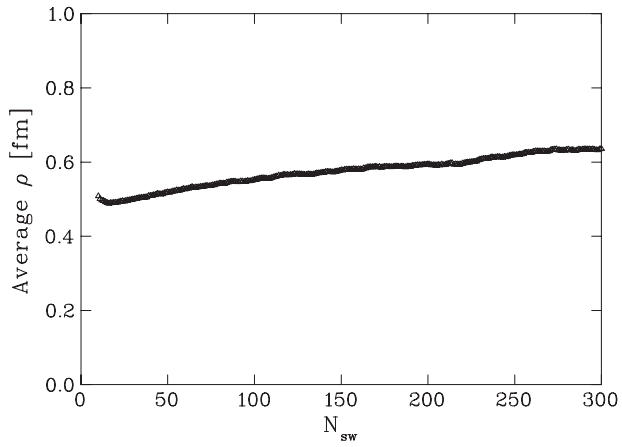

FIG. 4. Average fitted radius of instanton candidates, as a function of overimproved smearing sweeps.

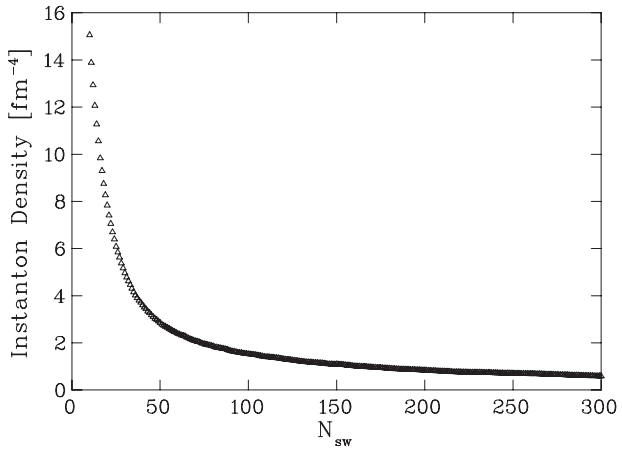

FIG. 5. Average density of instanton candidates on the lattice, as a function of overimproved smearing sweeps.

density of ≈ 2 fm^{-4} at this point. In the instanton liquid model, phenomenological constraints set the instanton radius to be around $\rho = \frac{1}{3}$ fm and density to $N = 1$ fm^{-4}, leading to a packing fraction, the proportion of the vacuum composed of instantons, of $NV_{\mathrm{inst}} = N\frac{\pi^2\rho^4}{2} = 0.05$. Here, $V_{\mathrm{inst}} = \frac{\pi^2\rho^4}{2}$ is the 4-volume of an instanton of radius ρ. On the lattice, we have found a density of between 0.4 fm^{-4} and 2 fm^{-4}, reaching an equivalent density to the instanton liquid model at approximately 160 sweeps of smearing. In the second half of this study, we use configurations with less than 100 sweeps of smearing, leading to a density much higher than used in the instanton liquid model.

In order to investigate this further, we have plotted the topological charge coherence, the proportion of lattice sites with topological charge of the same sign as at the center, within 50%, $C(r < 0.5\rho)$, and 100%, $C(r < \rho)$, of the fitted instanton radius, in Fig. 6. At 50% of the instanton radius, almost all sites are charge coherent after a relatively small number of smearing sweeps, whereas at 100% of instanton radius, only 85% of the sites are charge coherent, even after a large amount of smearing. This suggests that our

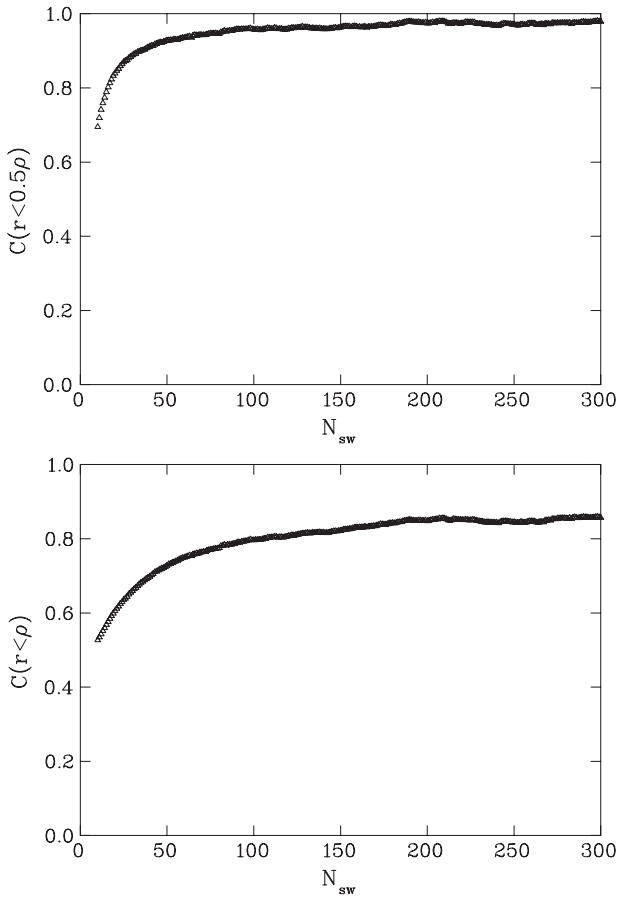

FIG. 6. The sign coherence, C, of topological charge density at the center of (anti-)instantons is explored as a function of smearing sweeps, N_{sw}. Plotted are the fraction of lattice sites within 50% (upper) and 100% (lower) of the fitted radius of an instanton candidates' center with topological charge of the same sign.

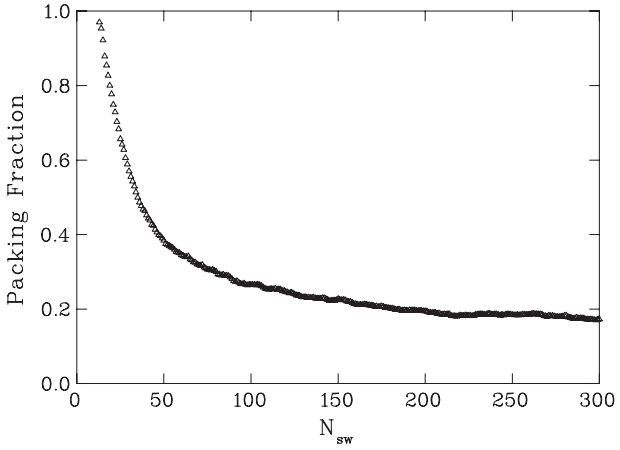

FIG. 7. Packing fraction of instantons, the percentage of the vacuum composed of instantons, as a function of smearing sweeps.

fitted values of ρ may be overestimating the true radius of instantons. We thus calculate the packing fraction using the topological charge found at the center and Eq. (11). This is plotted in Fig. 7. We note that a packing fraction exceeding 1 is not an issue, as instanton candidates may overlap, particularly at low levels of smearing. We find a packing fraction of between 0.15 and 0.3. Once again, this is notably higher than the instanton liquid model value of 0.05, suggesting that we have found a far "fuller" vacuum on the lattice.

Aggregating these measures, it is clear that between 50 and 100 sweeps of smearing gives an optimal balance, whereby the gauge field is dominated by instantons without excessive distortion. We will thus calculate quark propagators at 0, 30, 50, 80 and 100 sweeps of smearing.

IV. THE OVERLAP PROPAGATOR

The overlap fermion operator [21–24] is defined in the massless case by

$$D_o(0) = \frac{1}{2}(1 + \gamma_5 \epsilon(\gamma_5 D(m_w))), \tag{13}$$

with $\epsilon(A) = \frac{A}{\sqrt{A^2}}$ the matrix sign function, and the overlap kernel, $D(m_w)$, any reasonable Hermitian Dirac operator with mass parameter $-m_w$, governing the resolution of topologically nontrivial field structures [25,26]. The overlap is an explicit solution of the Ginsparg-Wilson relation [27],

$$\gamma_5 D_o + D_o \gamma_5 = 2 D_o \gamma_5 D_o, \tag{14}$$

and will thus have a lattice-deformed version of chiral symmetry. This is sufficient to prevent additive quark mass renormalization [28], greatly simplifying propagator analysis [29–31].

The massive overlap operator is then given by

$$D_o(\mu) = (1 - \mu) D_o(0) + \mu, \tag{15}$$

where the overlap mass parameter μ is defined to represent a bare quark mass

$$m_0 = 2 m_w \mu. \tag{16}$$

We use the FLIC action [32] as the overlap kernel, as studies have shown it to have superior spectral properties, accelerating calculation of the overlap operator, and reduced lattice discretization errors [12,33]. We project low modes of the kernel and calculate their contribution to the propagator explicitly, greatly reducing the condition number of the matrix square root.

Notably, we have found results consistent with the work of Neuberger [34], who predicts that in the presence of a sufficiently smooth background field, the eigenvalues of the Wilson kernel are maximally displaced from 0 at $m_w = 1$. In Fig. 8, we have plotted the 50 lowest lying eigenvalues of the FLIC kernel on a configuration with 50 sweeps of smearing and we observe that the region where the spectrum becomes dense (i.e. ignoring the isolated low-lying topological nodes) is indeed maximally separated from 0 near $m_w = 1$. We choose to perform all calculations at $m_w = 1$.

We consider nine values of μ, given in Table I.

In order to define an overlap quark propagator, we naturally wish to preserve the most important properties of the continuum propagator. As a simple consequence of chiral symmetry, in the massless case the continuum quark propagator obeys

$$\{\gamma_5, S^{\text{cont}}_{m=0}(p)\} = 0. \tag{17}$$

We also note that Eq. (14) implies

$$\{\gamma_5, D_o^{-1}\} = 2\gamma_5, \tag{18}$$

suggesting an appropriate form for the overlap propagator,

$$S(p)_{m=0} \propto (D_o^{-1} - 1). \tag{19}$$

It is also important to maintain the correct continuum limit, and so given

$$\lim_{a \to 0} D_o = \frac{1}{2m_w} \not{\partial}, \tag{20}$$

it is then natural to define the massless bare overlap propagator as [24,26]

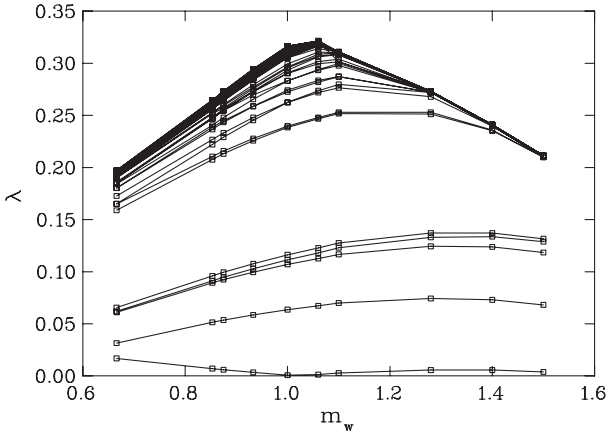

FIG. 8. The 50 lowest-lying eigenvalues of the overlap kernel as a function of kernel mass parameter m_w, from a single configuration with fifty sweeps of smearing.

TABLE I. The nine values of μ considered, with the corresponding bare mass in physical units.

μ	m_{bare} (MeV)
0.01271	39.8
0.01694	53.0
0.02119	66.4
0.02543	80.0
0.02966	93.0
0.03390	106.2
0.04238	132.7
0.05076	159.0
0.06356	199.1

$$S(p)_{m=0} = \frac{1}{2m_w}(D_o^{-1} - 1). \tag{21}$$

We can then construct the bare massive overlap propagator simply by adding a bare mass to the inverse of Eq. (21),

$$S(p)^{-1}_{m=m_0} = S(p)^{-1}_{m=0} + m_0, \tag{22}$$

then recalling the definition of the overlap mass parameter in Eq. (16), we have

$$S(p) = \frac{1}{2m_w(1-\mu)}(D_o^{-1} - 1). \tag{23}$$

Due to the lack of additive mass renormalization, the quark propagator on the lattice will have as its general form

$$S(p) = \frac{Z(p)}{i\not{q} + M(p)}, \tag{24}$$

with $M(p)$ the nonperturbative mass function and $Z(p)$ containing all renormalization information.

This can be defined as having the inverse

$$S^{-1}(p) \equiv i\sum_\mu (C_\mu(p)\gamma_\mu) + B(p) \equiv i\not{q}A(p) + B(p), \tag{25}$$

where $\not{q}$ is defined [30] by the tree level propagator, calculated with $U_\mu(x) = 1$,

$$S_0^{-1}(p) = i\not{q} + m_0. \tag{26}$$

Comparing Eq. (25) to Eq. (24), we see

$$Z(p) = \frac{1}{A(p)} \qquad M(p) = \frac{B(p)}{A(p)}. \tag{27}$$

Multiplying Eq. (25) by $\not{q}$ and taking the trace provides

$$A(p) = \frac{q_\mu C_\mu}{q^2}. \tag{28}$$

To determine $A(p)$ and $B(p)$ we follow Ref. [33] and define $\mathcal{C}$ and $\mathcal{B}$ by

$$S(p) = -i\mathcal{C}(p) + \mathcal{B}(p), \tag{29}$$

such that

$$\mathcal{B}(p) = \frac{1}{n_s n_c}\text{Tr}(S(p)) \quad \mathcal{C}_\mu(p) = \frac{i}{n_s n_c}\text{Tr}[\gamma_\mu S(p)], \tag{30}$$

where n_s and n_c are the extent of spin and color indices.

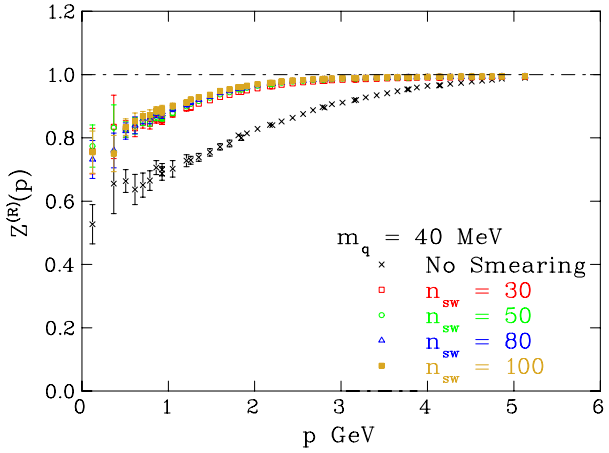

FIG. 9 (color online). The renormalization function at $m_q = 39.8$ MeV, on configurations with 0, 30, 50, 80, and 100 sweeps of smearing.

Comparing to Eq. (25), we find

$$C_\mu(p) = \frac{\mathcal{C}_\mu(p)}{\mathcal{C}^2(p) + \mathcal{B}^2(p)} \quad B(p) = \frac{\mathcal{B}(p)}{\mathcal{C}^2(p) + \mathcal{B}^2(p)}. \tag{31}$$

Defining

$$\mathcal{A}(p) = \frac{q_\mu \mathcal{C}_\mu}{q^2}, \tag{32}$$

we thus have

$$Z(p) = \frac{\mathcal{C}^2(p) + \mathcal{B}^2(p)}{\mathcal{A}(p)} \qquad M(p) = \frac{\mathcal{B}(p)}{\mathcal{A}(p)}. \tag{33}$$

V. RESULTS

We fix to Landau gauge by maximizing the $\mathcal{O}(a^2)$ improved gauge fixing functional [35]

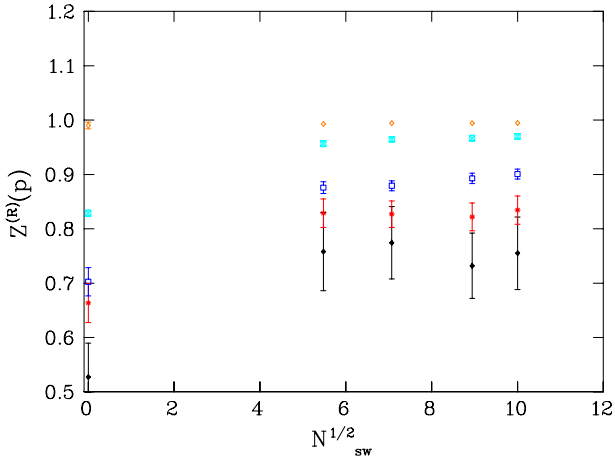

FIG. 10 (color online). The renormalization function plotted as a function of $N_{sw}^{1/2}$ at p values of 0.3, 0.6, 1, 2 and 5 GeV (ascending order), with $m_q = 40$ MeV.

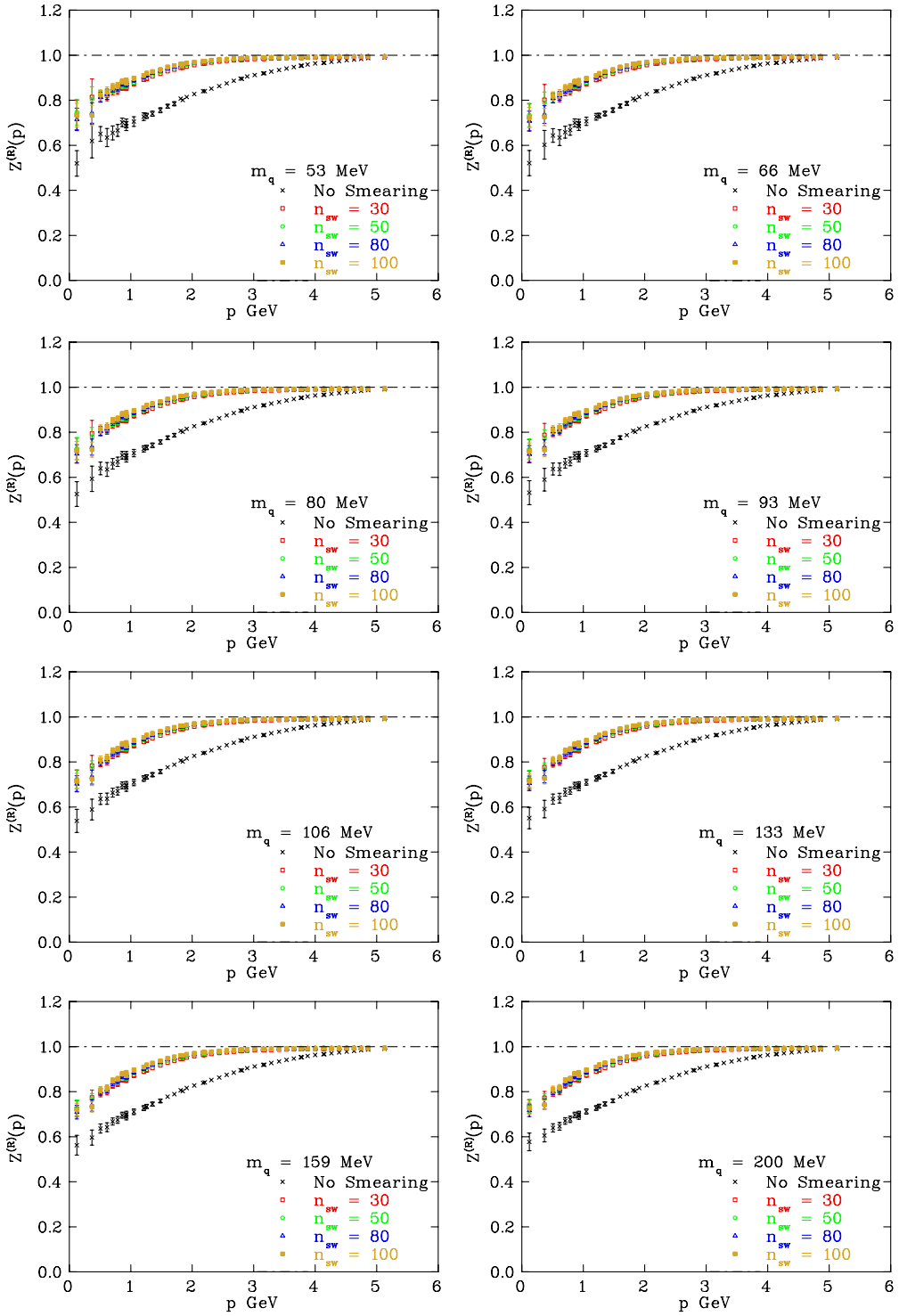

FIG. 11 (color online). The renormalization function at various values of m_q, on configurations with 0, 30, 50, 80, and 100 sweeps of smearing.

$$\mathcal{F}_{\text{imp}} = \sum_{x,\mu} \text{ReTr}\left(\frac{4}{3}U_\mu - \frac{1}{12u_0}(U_\mu(x)U(x+\hat{u}) + \text{H.c.})\right) \tag{34}$$

using a Fourier transform accelerated algorithm [35–38]. To avoid Gribov copy issues, we first gauge fix configurations with 100 sweeps of smearing and then use these as a preconditioner for the same configurations with lower levels of smearing [39]. The matrix sign function is calculated using the Zolotarev rational polynomial approximation [40]. We average data over spatial symmetries and choose $p = 5$ GeV as the renormalization point for

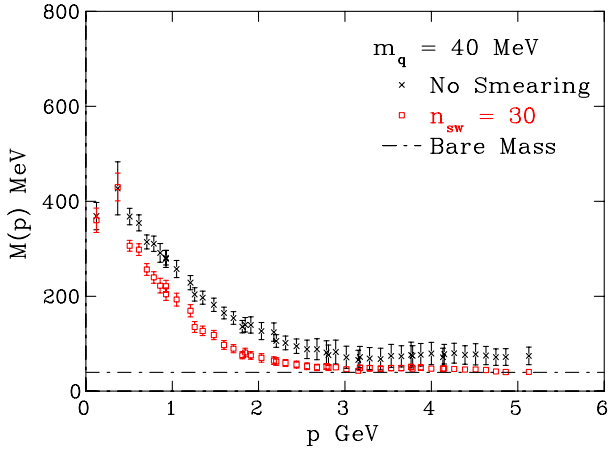

FIG. 12 (color online). The mass function at $m_q = 39.8$ MeV on unsmeared configurations and with 30 sweeps of smearing.

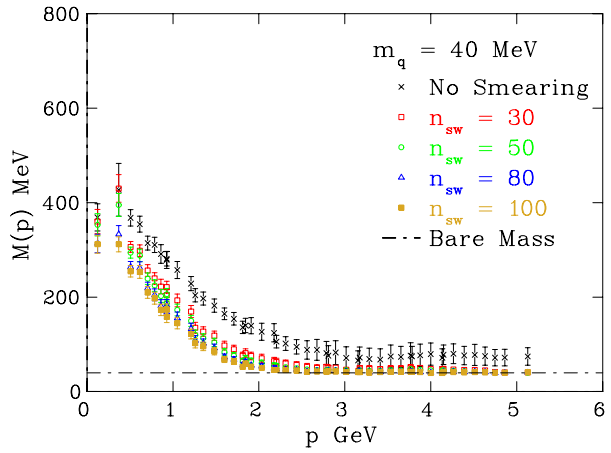

FIG. 13 (color online). The mass function at $m_q = 39.8$ MeV on unsmeared configurations and with 30, 50, 80 and 100 sweeps of smearing.

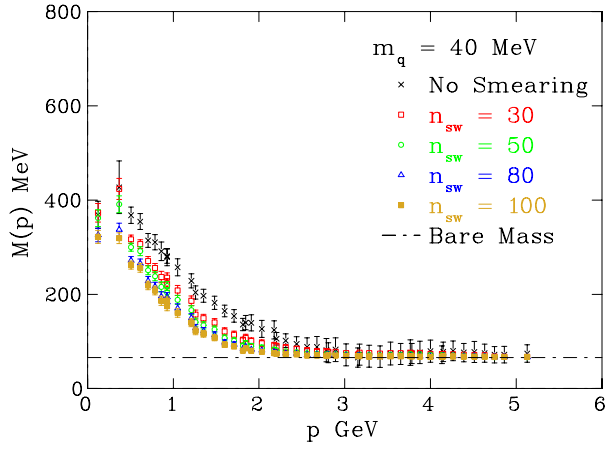

FIG. 14 (color online). The mass function at $\mu = 0.01271$ on unsmeared configurations and at $\mu = 0.02119$ on configurations with 30, 50, 80 and 100 sweeps of smearing.

$Z^{(\mathcal{R})}$, with $Z^{(\mathcal{R})}(p = 5\ \text{Gev}) = 1$. We apply a cylinder cut [30] to data with a radius of $\frac{\pi}{2a}$, and estimate errors using a second-order single-elimination jack-knife method.

$Z^{(\mathcal{R})}$ is plotted in Fig. 9 for the lightest quark mass, 39.8 MeV, for various levels of smearing. This reveals the well-known shape of the renormalization function for the unsmeared case, dipping in the infrared region and rising in the ultraviolet limit. After just 30 sweeps of smearing however, different behavior is seen. The renormalization function is more tree like, dipping half the amount and approximating 1 for $p > 3$ GeV. The renormalization function rises earlier to this plateau value, with similar behavior seen at all levels of smearing. This appears to confirm our earlier observations; after 30 sweeps most short-range behavior is removed, and the gauge field structure of the lattice is much simpler. The physics responsible for the drop in $Z^{(\mathcal{R})}$ is removed early as all curves agree.

To further show this, $Z^{(\mathcal{R})}$ is plotted as a function of $\sqrt{N_{sw}}$ at given values of p in Fig. 10. We have chosen to plot against $\sqrt{N_{sw}}$ as this is proportional to the smearing radius. This shows a large change from 0 to 30 sweeps of smearing, affirming that the physics responsible for the drop in $Z^{(\mathcal{R})}$ is removed early in the smearing process, after which smearing has relatively little effect.

Higher masses are illustrated for all p in Fig. 11. Remarkably little sensitivity to the quark mass is observed. We note that the lowest two p values are purely timelike, and thus have comparatively large error bars due to the lack of symmetries for averaging.

We now plot the mass function for a quark mass of 39.8 MeV in Fig. 12. The unsmeared data reveals the expected shape—a large effective quark mass in the infrared region created through dynamical mass generation, tapering to an approximate plateau in the ultraviolet region, where logarithmic corrections produce a running quark

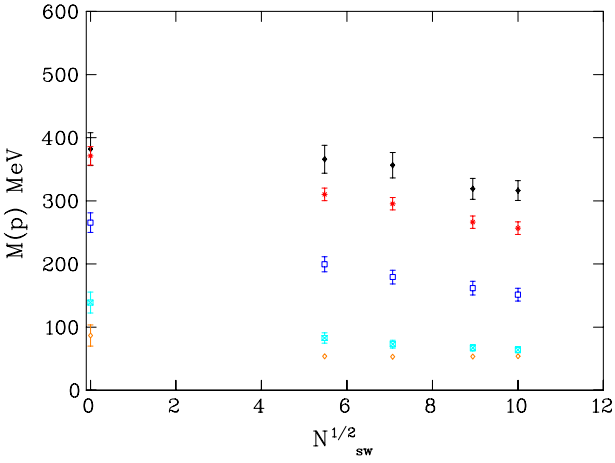

FIG. 15 (color online). The mass function plotted as a function of $N_{sw}^{1/2}$ at p values of 0.3, 0.6, 1, 2 and 5 GeV (descending order), with $m_q = 53$ MeV.

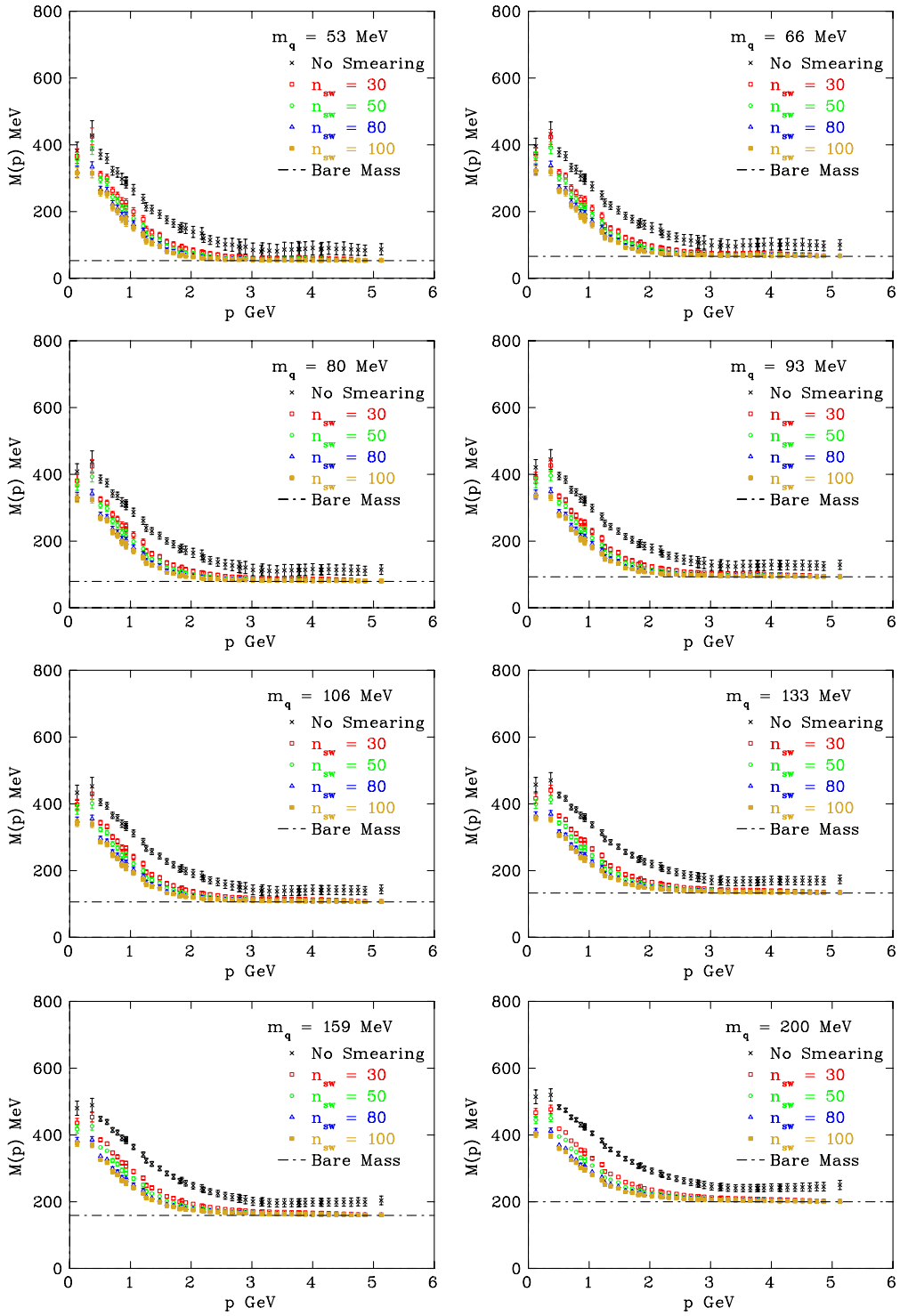

FIG. 16 (color online). The mass function at various values of bare quark mass, indicated by the dot-dash line. The same value of bare mass is used for both smeared and unsmeared results. Configurations with 0, 30, 50, 80 and 100 sweeps of smearing are considered.

mass higher than the input bare mass, illustrated by the dot-dash line.

Looking at the lowest level of smearing considered, 30 sweeps, we note that the smeared results consistently have smaller error bars, particularly in the ultraviolet region, indicating short distance physics is a significant source of noise. Although the instanton content of each ensemble is different, its impact on the mass function remains similar.

We also note that, as expected, in the ultraviolet region the running quark mass is now barely higher than the input bare mass, due to the spoiling of short distance perturbative physics at this range. At the lowest momenta, we find perfect agreement with the unsmeared case, but as we increase momentum there is some suppression of dynamically generated mass. We attribute this to the destruction of some topological objects by the smearing algorithm, both those smaller than the dislocation threshold and those eliminated by pair annihilation. Smearing also has the effect of enlarging objects, again removing dynamically generated mass from this region. Indeed one anticipates a significant smearing dependence in the regime of $p \approx 1$ GeV.

We now plot all levels of smearing, in Fig. 13. Even at high levels of smearing, we have maintained the qualitative shape of the mass function, although increasing smearing results in a larger loss of dynamically generated mass. As the level of smearing increases, the mass function becomes flat for lower values of momenta. This is in accord with the increase of the smearing radius, the distance within which physics is suppressed. The most dramatic shift is between the unsmeared case and 30 sweeps. This suggests that, to at least some extent, smearing has changed the mass renormalization, and so in order to acquire results with the same physical mass we must shift our value of μ for the smeared results.

In Fig. 14 we have plotted smeared results at a value of $\mu = 0.02119$, chosen in order to match unsmeared results in the ultraviolet limit. This reveals that not all loss of dynamical mass generation is due to a changing mass renormalization. Although we have retained the majority of long-range physics, it is clear that smearing, particularly after a large number of sweeps, has removed some important aspects of vacuum structure, creating a gap between unsmeared and smeared results.

$M(p)$ is plotted as a function of $\sqrt{N_{sw}}$ at fixed values of p in Fig. 15, for a quark mass of $m_q = 53$ MeV. This shows an approximately linear dependence on $\sqrt{N_{sw}}$ and thus the smearing radius.

This suggests that the increase in smearing radius is responsible for loss of dynamical mass generation by removing topological objects from the lattice. At higher momenta corresponding to smaller distances, smearing has removed all relevant physics from the lattice early, and so an increase in the smearing radius has a smaller effect.

Higher masses are shown in Fig. 16 for all p, using the same bare mass for both smeared and unsmeared configurations. These show broadly similar results at all masses, though the gap between levels of smearing becomes clearer for larger masses, which should be more sensitive to the disruption of short distance physics. This reinforces the necessity of maintaining a high density of topological objects in the QCD vacuum and reinforcing the danger of destroying topological objects with excess smearing. The largest gap, however, remains between no smearing and 30 sweeps.

VI. CONCLUSION

We have used over-improved stout-link smearing, to reveal an underlying gauge field structure resembling an instanton liquid. After around 50 sweeps we can be confident the lattice is dominated by instantonlike objects.

Our calculations of the nonperturbative mass function on smeared configurations reveals that it retains its qualitative shape at even high levels of smearing. There is some loss of dynamical mass generation, increasing with smearing, which can be attributed to a thinning of the vacuum through the destruction of instanton/anti-instanton pairs by the smearing algorithm. Regardless, we have shown that a gauge configuration consisting solely of instantonlike objects can accurately reproduce the majority of the long-range behavior of the quark propagator, and thus conclude that instantons are the primary mechanism responsible for the dynamical generation of mass.

ACKNOWLEDGMENTS

We wish to thank Craig Roberts for discussions inspiring this quantitative evaluation of the role of QCD instantons in the quark propagator. We also thank Peter Moran for his input. This research was undertaken with the assistance of resources at the NCI National Facility in Canberra, Australia, and the iVEC facilities at Murdoch University (iVEC@Murdoch) and the University of Western Australia (iVEC@UWA). These resources were provided through the National Computational Merit Allocation Scheme, supported by the Australian Government. This research is supported by the Australian Research Council.

[1] B. Berg, Phys. Lett. **104B**, 475 (1981).
[2] M. Teper, Phys. Lett. **162B**, 357 (1985).
[3] E. -M. Ilgenfritz, M. L. Laursen, G. Schierholz, M. Muller-Preussker, and H. Schiller, Nucl. Phys. **B268**, 693 (1986).
[4] M. Albanese *et al.* (APE Collaboration), Phys. Lett. B **192**, 163 (1987).
[5] A. Hasenfratz and F. Knechtli, Phys. Rev. D **64**, 034504 (2001).
[6] C. Morningstar and M. J. Peardon, Phys. Rev. D **69**, 054501 (2004).
[7] M. Garcia Perez, A. Gonzalez-Arroyo, J. R. Snippe, and P. van Baal, Nucl. Phys. **B413**, 535 (1994).

[8] P. J. Moran and D. B. Leinweber, Phys. Rev. D **77**, 094501 (2008).
[9] E. V. Shuryak, Nucl. Phys. **B203**, 93 (1982).
[10] E. V. Shuryak, Nucl. Phys. **B203**, 116 (1982).
[11] E. V. Shuryak, Nucl. Phys. **B203**, 140 (1982).
[12] W. Kamleh, D. H. Adams, D. B. Leinweber, and A. G. Williams, Phys. Rev. D **66**, 014501 (2002).
[13] T. G. Kovacs, Phys. Rev. D **62**, 034502 (2000).
[14] A. A. Belavin, A. M. Polyakov, A. S. Schwartz, and Y. .S. Tyupkin, Phys. Lett. **59B**, 85 (1975).
[15] D.-J. Kusterer, J. Hedditch, W. Kamleh, D. B. Leinweber, and A. G. Williams, Nucl. Phys. **B628**, 253 (2002).
[16] G. 't Hooft, Phys. Rev. Lett. **37**, 8 (1976).
[17] G. 't Hooft, Phys. Rev. D **14**, 3432 (1976) [**18**, 2199(E) (1978)].
[18] K. Symanzik, Nucl. Phys. **B226**, 187 (1983).
[19] P. J. Moran and D. B. Leinweber, Phys. Rev. D **78**, 054506 (2008).
[20] S. O. Bilson-Thompson, F. D. R. Bonnet, D. B. Leinweber, and A. G. Williams, Nucl. Phys. B, Proc. Suppl. **109**, 116 (2002).
[21] R. Narayanan and H. Neuberger, Phys. Lett. B **302**, 62 (1993).
[22] R. Narayanan and H. Neuberger, Nucl. Phys. **B412**, 574 (1994).
[23] R. Narayanan and H. Neuberger, Phys. Rev. Lett. **71**, 3251 (1993).
[24] R. Narayanan and H. Neuberger, Nucl. Phys. **B443**, 305 (1995).
[25] P. J. Moran, D. B. Leinweber, and J. Zhang, Phys. Lett. B **695**, 337 (2011).
[26] R. G. Edwards, U. M. Heller, and R. Narayanan, Phys. Rev. D **59**, 094510 (1999).
[27] P. H. Ginsparg and K. G. Wilson, Phys. Rev. D **25**, 2649 (1982).
[28] P. Hasenfratz, Nucl. Phys. **B525**, 401 (1998).
[29] J. Skullerud, D. B. Leinweber, and A. G. Williams, Phys. Rev. D **64**, 074508 (2001).
[30] F. D. R. Bonnet, P. Bowman, D. Leinweber, A. Williams, and J. Zhang (CSSM Lattice Collaboration), Phys. Rev. D **65**, 114503 (2002).
[31] J. I. Skullerud and A. G. Williams, Phys. Rev. D **63**, 054508 (2001).
[32] J. M. Zanotti, S. Bilson-Thompson, F. Bonnet, P. Coddington, D. Leinweber, A. Williams, J. Zhang, W. Melnitchouk, and F. Lee (CSSM Lattice Collaboration), Phys. Rev. D **65**, 074507 (2002).
[33] W. Kamleh, P. O. Bowman, D. B. Leinweber, A. G. Williams, and J. Zhang, Phys. Rev. D **71**, 094507 (2005).
[34] H. Neuberger, Phys. Rev. D **61**, 085015 (2000).
[35] C. T. H. Davies, G. Batrouni, G. Katz, A. Kronfeld, G. Lepage, K. Wilson, P. Rossi, and B. Svetitsky, Phys. Rev. D **37**, 1581 (1988).
[36] D. S. Roberts, W. Kamleh, and D. B. Leinweber, Proc. Sci., LATTICE 2012 (2012) 261.
[37] D. S. Roberts, P. O. Bowman, W. Kamleh, and D. B. Leinweber, Phys. Rev. D **83**, 094504 (2011).
[38] F. D. R. Bonnet, P. O. Bowman, D. B. Leinweber, A. G. Williams, and D. G. Richards, Aust. J. Phys. **52**, 939 (1999).
[39] J. E. Hetrick and P. de Forcrand, Nucl. Phys. B, Proc. Suppl. **63**, 838 (1998).
[40] T.-W. Chiu, T.-H. Hsieh, C.-H. Huang, and T.-R. Huang, Phys. Rev. D **66**, 114502 (2002).